Self-dual $CP(2)$ vortex-like solitons in the presence of magnetic impurities

V. Almeida[*] and R. Casana[†]

Departamento de Física, Universidade Federal do Maranhão, 65080-805, São Luís, Maranhão, Brazil

E. da Hora[‡]

Coordenação do Curso de Bacharelado Interdisciplinar em Ciência e Tecnologia, Universidade Federal do Maranhão, 65080-805, São Luís, Maranhão, Brazil

S. Krusch[§]

School of Mathematics, Statistics and Actuarial Science, University of Kent, Canterbury, CT2 7FS, United Kingdom

(Received 18 May 2021; accepted 12 July 2022; published 25 July 2022)

We investigate the existence of vortex configurations in two gauged-$CP(2)$ models extended via the inclusion of magnetic impurities. In particular, we consider both the Maxwell-$CP(2)$ and the Chern-Simons-$CP(2)$ enlarged scenarios, separately. We choose a $CP(2)$-field configuration with a null topological charge not only in the simplest (free) case, but also when coupled to an Abelian gauge field. The implementation of the Bogomol'nyi-Prasad-Sommerfield (BPS) formalism shows that the effective models for such a configuration possess a self-dual structure which looks like those inherent to the gauged sigma models. Therefore, when the $CP(2)$ field is coupled to the Maxwell term, the corresponding total energy possesses both a well-defined Bogomol'nyi bound and a quantized magnetic flux. Further, when the $CP(2)$ scenario is gauged with the Chern-Simons action, the total electric charge is verified to be proportional to the quantized magnetic flux. In addition, the analysis verifies that the magnetic impurity contributes to the BPS potentials and appears in both of the models' BPS equations. Next, we introduce a Gaussian-type impurity and solve the self-dual equations via a finite-difference scheme. The resulting solutions present a nonmonotonic behavior that flips both the magnetic and electric fields. Finally, we discuss the topologically trivial solutions in the limit for which the impurity becomes a Dirac δ function.

DOI: 10.1103/PhysRevD.106.016010

I. INTRODUCTION

Configurations with nontrivial topology are usually achieved as the solutions of the Euler-Lagrange equations which appear in the context of nonlinear field theories [1]. In this case, the nonlinearity originates from a potential term that promotes the spontaneous breaking of the original model's symmetry. However, the resulting second-order Euler-Lagrange equations are highly nonlinear and usually quite hard to solve.

Under exceptional circumstances, topological solutions can also be obtained via a particular set of first-order differential equations, the so-called Bogomol'nyi-Prasad-Sommerfield (BPS) ones. It is interesting to note that these equations emerge as a result of the implementation of the Bogomol'nyi technique, which stands for the minimization of the total energy inherent to the field model [2]. Among the algorithms that lead to the BPS equations, we can include the study of the conservation of the corresponding energy-momentum tensor [3] and the on-shell method [4]. In such a scenario, the simplest BPS gauged vortices occur in the Maxwell-Higgs [5], Chern-Simons-Higgs [6], and Maxwell-Chern-Simons-Higgs [7] theories.

More recently, it was shown that first-order or BPS vortices also exist in a gauged scenario that describes the interaction between the Maxwell and the $CP(2)$ fields [8,9]. Besides that, some of us have also studied the existence of BPS vortices in the Chern-Simons-$CP(2)$ [10], and in the Maxwell-Chern-Simons-$CP(2)$ [11] models. BPS vortices also arise in the context of extended scenarios based on a gauged-$CP(2)$ model, as the Maxwell-$CP(2)$ vortices saturated by a nontrivial dielectric function [12] and the Maxwell-$CP(2)$ vortices with internal structures due to the presence of an additional scalar field [13].

[*]vinicius.marcos@discente.ufma.br
[†]rodolfo.casana@ufma.br; rodolfo.casana@gmail.com
[‡]carlos.hora@ufma.br; edahora.ufma@gmail.com
[§]S.Krusch@kent.ac.uk

The interactions between vortices and impurities have been observed in various physical systems (such as condensed matter [14], Bose-Einstein condensates [15], and neutron stars [16]), with their dynamics explored, for instance, in Refs. [17,18]. More recently, a systematic way to introduce impurities into BPS systems (which leads to the preservation of half of the BPS equations) was developed in Refs. [19,20]. Such a procedure allows the detailed investigation of, for example, the scattering of a kink by a kink which is trapped by an impurity; see also the Ref. [21] for an earlier study. Moreover, an open question is how the impurities affect the Manton-Schrödinger-Chern-Simons model [22] and its interesting vortex dynamics [23,24].

On the other hand, a promising physical issue is the search for regular solitons inherent to enlarged field theories which mimic condensed matter phenomena. In this sense, the first studies about the existence of BPS vortices in a Maxwell-Higgs scenario enlarged by impurities (both magnetic and electric) were done by Tong and Wong [25] and showed how the presence of impurities affects the corresponding moduli space. Moreover, in Ref. [26], the authors proposed existence theorems for both vortices and antivortices in the presence of magnetic impurities. In the sequence, first-order vortices inherent to a Chern-Simons-Higgs model extended to include impurities were obtained in Ref. [27]. Furthermore, some of us investigated the interaction between a moving Maxwell-Higgs vortex and a static magnetic impurity; see Refs. [28,29].

We now go further and study the occurrence of BPS vortex-like solutions in the context of gauged $CP(2)$ models in the presence of magnetic impurities. More specifically, we consider those topological structures engendered by the following $CP(2)$ configuration:

$$\phi = \begin{pmatrix} (-1)^k \psi \\ \psi^* \\ \phi_3 \end{pmatrix}, \qquad |\phi|^2 = h, \tag{1}$$

where $k \in \mathbb{Z}$, with $\psi \in \mathbb{C}$ and $\phi_3 \in \mathbb{R}$. The configuration above is related to the $CP(2)$ solutions studied in Refs. [8–11] (in particular, the configuration with $\beta_1 = \frac{\pi}{4} + \frac{\pi k}{2}$ considered there). It is easy to verify that the configuration (1) has a null $CP(2)$ topological charge; see Eqs. (4) and (7) below. In addition, this $CP(2)$ configuration, when minimally coupled to the Abelian gauge field, possesses a well-defined BPS structure (see Secs. II and IV below) which supports the vortex-like solutions studied in Refs. [8–11].

Here, it is worthwhile to point out that the $CP(N)$ field describes topological excitations in some cold atomic systems. For example, in the $s = 1/2$ fermion case, the $CP(1)$ model describes the spin dynamics [30], whereas the $CP(3)$ model can be used to study the $s = 3/2$ case [31]. We then expect that the $CP(2)$ configuration (1) would describe excitations of a spin-1 Bose-Einstein condensate such as vortices or monopoles [32–34].

The present manuscript considers those effective scenarios for the configuration (1) which arise from both the Maxwell-$CP(2)$ and the Chern-Simons-$CP(2)$ models now enlarged to include a localized impurity, which is rotationally symmetric. We organize our work as follows. In Sec. II, we study the BPS structure of the effective Maxwell-$CP(2)$ model for the configuration (1). In Sec. III, we introduce an extended Maxwell-$CP(2)$ theory saturated by an additional term which stands for the impurity itself. We then look for vortex-like solutions which minimize the total energy via the implementation of the so-called BPS prescription, from which we obtain not only a well-defined energy lower bound, but also the self-dual equations whose solutions saturate that bound. We point out the main differences between the resulting solutions and the ones obtained without impurities by discussing how the impurity affects the formation of the corresponding vortices. In Sec. IV, the BPS structure of the effective Chern-Simons-$CP(2)$ model engendered by the configuration (1) is analyzed. In addition, Sec. V is dedicated to the study of the enlarged Chern-Simons-$CP(2)$ scenario. Here, for the sake of convention, we discuss the theoretical construction in detail by comparing it to the case considered in the previous Sec. III. Finally, Sec. VI contains our conclusions and perspectives regarding future contributions.

II. EFFECTIVE MAXWELL-$CP(2)$ MODEL

The Maxwell-$CP(2)$ model is described by the following Lagrangian density [35]:

$$\mathcal{L} = -\frac{1}{4} F_{\mu\nu} F^{\mu\nu} + (\nabla_\mu \phi)^\dagger (\nabla^\mu \phi) - U(\phi), \tag{2}$$

where ϕ is the $CP(2)$ field, which possesses three complex components which satisfy the normalization condition $\phi^\dagger \phi = h$. The topological current density inherent to the $CP(2)$ field is given by

$$\tau_\mu = \frac{1}{2\pi i h} \varepsilon_{\mu\nu\rho} (\mathcal{D}^\nu \phi)^\dagger (\mathcal{D}^\rho \phi), \tag{3}$$

where $\mathcal{D}_\mu \phi = \partial_\mu \phi - h^{-1} (\phi^\dagger \partial_\mu \phi) \phi$, with the resulting topological charge being expressed as

$$\mathrm{q} = \int d^2\mathbf{x}\, \tau_0 \in \mathbb{Z} \backslash \{0\}. \tag{4}$$

Moreover, in Eq. (2), $F_{\mu\nu} = \partial_\mu A_\nu - \partial_\nu A_\mu$ stands for the usual field-strength tensor of the $U(1)$ gauge field A_μ, which is minimally coupled to the $CP(2)$ sector via the covariant derivative $\nabla_\mu \phi = D_\mu \phi - h^{-1} (\phi^\dagger D_\mu \phi) \phi$. Here, $D_\mu \phi$ is given by

$$D_\mu\phi = \partial_\mu\phi - igA_\mu\mathbb{Q}\phi, \tag{5}$$

where g represents an electromagnetic coupling constant and $\mathbb{Q}$ stands for a real charge matrix (diagonal and traceless). The topological current density of the gauged $CP(2)$ reads

$$T_\mu = \frac{1}{2\pi ih}\epsilon_{\mu\nu\rho}\left[(\nabla^\nu\phi)^\dagger(\nabla^\rho\phi) - \frac{ig}{2}F^{\nu\rho}(\phi^\dagger\mathbb{Q}\phi)\right], \tag{6}$$

with its topological charge being given by

$$\mathfrak{Q} = \int d^2\mathbf{x}\, T_0 \in \mathbb{Z}\backslash\{0\}. \tag{7}$$

As mentioned previously, the $CP(2)$ configuration (1) possesses a null topological charge in both the free case (4) and the gauged case (7) where the charge matrix $\mathbb{Q}$ is given by [8]

$$\mathbb{Q} = \frac{1}{2}\mathrm{diag}(1,-1,0), \tag{8}$$

which is related to the matrix $\lambda_3 = \mathrm{diag}(1,-1,0)$, i.e., one of the Gell-Mann matrices which represent the $SU(3)$ group.

In the remainder of the present section, we will show that the effective model for the configuration (1) obtained from the original theory (2) supports a well-defined BPS structure. Thus, the Lagrangian density that describes the effective model is

$$\mathcal{L} = -\frac{1}{4}F_{\mu\nu}F^{\mu\nu} + (D_\mu\phi)^\dagger D^\mu\phi - U_0(\phi_3) - \lambda(h - \phi^\dagger\phi), \tag{9}$$

where ϕ represents the configuration (1) and the covariant derivative $D_\mu\phi$ is defined in Eq. (5). Also, λ stands for a Lagrange multiplier which guarantees the condition $h = \phi^\dagger\phi = 2|\psi|^2 + (\phi_3)^2$.

The field equation for the gauge sector reads

$$\partial_\nu F^{\nu\mu} = J^\mu, \tag{10}$$

where J^μ is the conserved current density related to the charged field ψ, with its expression being

$$J^\mu = ig[(\hat{D}^\mu\psi)^*\psi - \psi^*\hat{D}^\mu\psi], \tag{11}$$

with the quantity $\hat{D}^\mu\psi$ standing for the corresponding covariant derivative, i.e.,

$$\hat{D}_\mu\psi = \partial_\mu\psi - \frac{ig}{2}A_\mu\psi. \tag{12}$$

On the other hand, the field equation for the charged sector ψ itself is

$$\hat{D}_\mu\hat{D}^\mu\psi - \lambda\psi = 0, \tag{13}$$

while that for the neutral field ϕ_3 reads

$$\partial_\mu\partial^\mu\phi_3 + \frac{1}{2}\frac{\partial U_0}{\partial\phi_3} - \lambda\phi_3 = 0. \tag{14}$$

Via the combination between the last two equations and the relation $h = 2|\psi|^2 + (\phi_3)^2$, we additionally attain the following expression for the Lagrange multiplier λ:

$$h\lambda = -2|\hat{D}_\mu\psi|^2 - (\partial_\mu\phi_3)^2 + \frac{1}{2}\phi_3\frac{\partial U_0}{\partial\phi_3}. \tag{15}$$

We now write down the equations for stationary fields. In this sense, Eq. (10) leads to the Gauss law

$$\partial_k\partial_k A_0 = g^2 A_0|\psi|^2, \tag{16}$$

which is identically satisfied by the gauge condition $A^0 = 0$. This condition therefore stands for the gauge choice that we use throughout the rest of this section. Hence, we conclude that the stationary solutions inherent to the model (9) present zero total charge and carry only magnetic flux.

Ampère's law becomes

$$\epsilon_{kj}\partial_j B = -J_k, \tag{17}$$

while the stationary equations for the fields ψ and ϕ_3 are

$$\hat{D}_k\hat{D}_k\psi + \lambda\psi = 0, \tag{18}$$

$$\partial_k\partial_k\phi_3 - \frac{1}{2}\frac{\partial U_0}{\partial\phi_3} + \lambda\phi_3 = 0, \tag{19}$$

with λ now written as

$$h\lambda = 2|\hat{D}_k\psi|^2 + (\partial_k\phi_3)^2 + \frac{1}{2}\phi_3\frac{\partial U_0}{\partial\phi_3}. \tag{20}$$

A. BPS structure of the model described by the configuration (1)

The stationary energy density of the model (9) is

$$\varepsilon = \frac{1}{2}B^2 + (D_k\phi)^\dagger D_k\phi + U_0(\phi_3), \tag{21}$$

where we have used the gauge condition $A_0 = 0$. The corresponding total energy is given by

$$\mathcal{E} = \int d^2\mathbf{x}\varepsilon. \tag{22}$$

In order to implement the BPS formalism, we consider the relations

$$\frac{1}{2}B^2 = \frac{1}{2}(B \mp \sqrt{2U_0})^2 \pm B\sqrt{2U_0}, \tag{23}$$

and

$$|D_k\phi|^2 = \frac{1}{2}|D_j\phi \pm ih^{-1/2}\epsilon_{jk}(\phi \times D_k\phi)^*|^2 \mp ih^{-1/2}\epsilon_{jk}\phi \cdot (D_j\phi \times D_k\phi), \tag{24}$$

via which we rewrite the total energy in the form

$$\mathcal{E} = \int d^2\mathbf{x}\left\{\frac{1}{2}|D_j\phi \pm ih^{-1/2}\epsilon_{jk}(\phi \times D_k\phi)^*|^2 + \frac{1}{2}(B \mp \sqrt{2U_0})^2 \pm B(\sqrt{2U_0} - h^{1/2}g\phi_3) \mp \frac{i}{h^{1/2}}[\epsilon_{jk}\phi \cdot (D_j\phi \times D_k\phi) + ihg\phi_3 B]\right\}. \tag{25}$$

Now, if we consider $B = -F_{12} = -\epsilon_{jk}\partial_j A_k$, the last term in the equation above can be related to the zeroth component of the topological current density of the model, i.e.,

$$\bar{q}_\mu = \frac{\epsilon_{\mu\nu\lambda}}{i2\pi h^{3/2}}\left[\phi \cdot (D^\nu\phi \times D^\lambda\phi) - ih\frac{g}{2}\phi_3 F^{\nu\lambda}\right], \tag{26}$$

whose integration provides the topological charge

$$\int d^2\mathbf{x}\bar{q}_0 \in \mathbb{Z}\backslash\{0\}, \tag{27}$$

from which we conclude that the integration of the term in the third row of Eq. (25) provides the system's BPS energy in terms of the topological charge, i.e.,

$$\mathcal{E}_{bps} = \pm 2\pi h\int d^2\mathbf{x}\bar{q}_0 > 0. \tag{28}$$

In the second row of Eq. (25), we choose the factor which multiplies the magnetic field as zero, from which we obtain the BPS potential

$$U_0 = \frac{1}{2}hg^2(\phi_3)^2. \tag{29}$$

In view of the two last equations, the total energy then becomes

$$\mathcal{E} = \mathcal{E}_{bps} + \frac{1}{2}\int d^2\mathbf{x}(B \mp h^{1/2}g\phi_3)^2 + \frac{1}{2}\int d^2\mathbf{x}|D_j\phi \pm ih^{-1/2}\epsilon_{jk}(\phi \times D_k\phi)^*|^2, \tag{30}$$

from which we see that the total energy satisfies

$$\mathcal{E} \geq \mathcal{E}_{bps}, \tag{31}$$

with the equality being satisfied when the quadratic terms which appear within the integrals are chosen to be zero. This choice provides the BPS or self-dual equations of the system, i.e.,

$$B = \pm h^{1/2}g\phi_3, \tag{32}$$

$$D_j\phi = \mp ih^{-1/2}\epsilon_{jk}(\phi \times D_k\phi)^*, \tag{33}$$

which resemble those obtained in the context of the gauged $O(3)$ sigma model. Indeed, the BPS configurations can be considered as the classical solutions related to an extended supersymmetric version [36,37] of the model (9).

In particular, the second BPS equation can be rewritten in terms of the field components which appear in Eq. (1). We then get

$$\hat{D}_j\psi = \mp ih^{-1/2}\epsilon_{jk}(\psi\partial_k\phi_3 - \phi_3\hat{D}_k\psi), \tag{34}$$

$$\partial_j\phi_3 = \pm h^{-1/2}g^{-1}\epsilon_{jk}J_k, \tag{35}$$

where J_k is the conserved current density defined previously in Eq. (11).

In the BPS limit, the self-dual equations recover the stationary Ampère's law (17) and the stationary Euler-Lagrange equations for the fields ψ [Eq. (18)] and ϕ_3 [Eq. (19)].

On the other hand, the solutions of the BPS equations describing radially symmetric vortices were recently studied in Refs. [8,9], for the case $\beta = \beta_1$.

III. MAXWELL-*CP*(2) VORTEX-LIKE SOLITONS IN THE PRESENCE OF A MAGNETIC IMPURITY

We begin this work by defining the first model we will investigate. It consists of a Maxwell-$CP(2)$ theory extended to include an additional term representing the presence of a magnetic impurity. The resulting Lagrange density describing the enlarged model is

$$\mathcal{L} = -\frac{1}{4}F_{\mu\nu}F^{\mu\nu} + (D_\mu\phi)^\dagger(D^\mu\phi) - U(\phi_3, \Delta) + \Delta B, \tag{36}$$

where ϕ stands for the $CP(2)$ field configuration defined in Eq. (1).

The third term in Eq. (36) is the potential $U = U(\phi_3, \Delta)$ which also depends on the function Δ (the so-called *magnetic impurity*). The last term couples the magnetic field B to the impurity Δ which, in our analysis, depends explicitly on the spatial coordinates [i.e., $\Delta = \Delta(|\mathbf{x}|)$] and therefore breaks the translational invariance of the model. This breaking is not a problem if we consider the model (36) as an effective one. The point here is that the function

Δ represents a magnetic impurity in a medium where vortices exist; see the arguments in Ref. [25].

The equation for the gauge field is given by

$$\partial_\nu F^{\nu\mu} + (\delta_2^\mu \partial_1 \Delta - \delta_1^\mu \partial_2 \Delta) = J^\mu, \tag{37}$$

where J^μ is the current density (11).

We highlight that the presence of the term ΔB in Eq. (36) does not change the structure of the Gauss law obtained in the context of the usual Maxwell-$CP(2)$ model (9) *without* the magnetic impurity; see Ref. [9]. In this sense, the stationary Gauss law is still given by Eq. (16). As a consequence, we conclude that the stationary solutions inherent to the model (36) also present no electric charge and only carry magnetic flux.

We thus focus our attention on those time-independent configurations with rotational symmetry which transport only magnetic flux, from which we use the map

$$A_i = -\frac{\epsilon_{ij} x_j}{gr^2} A(r), \tag{38}$$

$$\psi = \sqrt{\frac{h}{2}} e^{im\theta} \sin\alpha(r) \quad \text{and} \quad \phi_3 = \sqrt{h}\cos\alpha(r), \tag{39}$$

where ϵ_{ij} stands for the two-dimensional Levi-Civita symbol (with $\epsilon_{12} = +1$), r and θ represent the polar coordinates, and $m \in \mathbb{Z}\backslash\{0\}$ is the winding number of the resulting configuration.

Under the parametrization (38) the magnetic field reads

$$B(r) = -\frac{1}{gr}\frac{dA}{dr}. \tag{40}$$

Both profile functions $A(r)$ and $\alpha(r)$, which depend only on the radial coordinate, must describe regular configurations with finite energy, from which they are supposed to satisfy the usual boundary conditions, i.e.,

$$\alpha(r=0) = 0 \quad \text{and} \quad A(r=0) = 0, \tag{41}$$

$$\alpha(r\to\infty) \to \frac{\pi}{2} \quad \text{and} \quad A(r\to\infty) \to 2m. \tag{42}$$

We now look for the first-order framework inherent to the model (36) through the standard BPS prescription, i.e., via the minimization of the enlarged model's total energy. The starting point is the expression for the corresponding energy distribution. In this sense, given the rotationally symmetric map (38) and (39) and all of the conventions introduced above, the time-independent energy density can be written in the form

$$\varepsilon = \frac{1}{2}B^2 + U(\alpha,\Delta) - \Delta B + h\left(\frac{d\alpha}{dr}\right)^2 + h\frac{(2m-A)^2}{4r^2}\sin^2\alpha, \tag{43}$$

from which one gets the total energy $\mathcal{E}$ as

$$\frac{\mathcal{E}}{2\pi} = \int_0^\infty \left[\frac{1}{2}B^2 + U(\alpha,\Delta) - \Delta B + h\left(\frac{d\alpha}{dr}\right)^2 + h\frac{(2m-A)^2}{4r^2}\sin^2\alpha\right] r dr. \tag{44}$$

After some algebra, the implementation of the BPS formalism leads to the following expression for the total energy:

$$\frac{\mathcal{E}}{2\pi} = \int_0^\infty \left[h\left(\frac{d\alpha}{dr} \pm \frac{(2m-A)}{2r}\sin\alpha\right)^2 + \frac{1}{2}(B \mp \sqrt{2U})^2 \pm 2\pi h\bar{q}_0 \pm B(\sqrt{2U} - gh\cos\alpha \mp \Delta)\right] r dr, \tag{45}$$

in which we have used the expression (40) for the magnetic field to attain the third and fourth terms. The quantity $\bar{q}_0$ is the topological charge density defined from Eq. (26), which expressed in polar coordinates reads

$$\bar{q}_0 = \frac{1}{2\pi r}\frac{d}{dr}[(2m-A)\cos\alpha]. \tag{46}$$

To complete the implementation of the BPS prescription, we set to zero the expression multiplying the magnetic field in the third row of Eq. (45). It fixes the BPS potential of the enlarged model, in terms of both the profile $\alpha(r)$ and the impurity $\Delta(r)$ itself, as

$$U(\alpha,\Delta) = \frac{g^2h^2}{2}\left(\cos\alpha \pm \frac{\Delta}{gh}\right)^2, \tag{47}$$

where both the potential and the function Δ vanish when $r\to\infty$.

Thus, by considering the relation (47), we then write the total energy (45) as

$$\frac{\mathcal{E}}{2\pi} = \frac{\mathcal{E}_{bps}}{2\pi} + \frac{1}{2}\int_0^\infty \left[B \mp gh\left(\cos\alpha \mp \frac{\Delta}{gh}\right)\right]^2 r dr + h\int_0^\infty \left[\frac{d\alpha}{dr} \pm \frac{(2m-A)}{2r}\sin\alpha\right]^2 r dr, \tag{48}$$

where $\mathcal{E}_{bps}$ is defined by Eq. (28) with $\bar{q}_0$ given in Eq. (46). So, the quantity $\mathcal{E}_{bps}$ stands for the lower bound (i.e., the Bogomol'nyi bound) of the total energy of the rotationally symmetric configurations. The particular value of the Bogomol'nyi bound can be calculated by using the boundary conditions (41) and (42). Therefore, the BPS energy for the model (36) becomes

$$\mathcal{E}_{bps} = \mp 4\pi h m > 0, \tag{49}$$

where the upper (lower) sign holds for negative (positive) values of the winding number m.

Therefore, from Eq. (48), it is possible to note that the total energy of the system satisfies the inequality

$$\mathcal{E} \geq \mathcal{E}_{bps}, \tag{50}$$

with the lower bound attained when the fields satisfy the so-called BPS equations, i.e.,

$$B = \pm gh\left(\cos\alpha \pm \frac{\Delta}{gh}\right), \tag{51}$$

$$\frac{d\alpha}{dr} = \mp \frac{(2m - A)}{2r}\sin\alpha, \tag{52}$$

whose solutions are rotationally symmetric structures with total energy equal to

$$\mathcal{E} = \mathcal{E}_{bps} = 4\pi h|m|. \tag{53}$$

Note that the value in Eq. (53) is quantized according to the winding number m, which is expected for topological configurations. We also highlight that the Bogomol'nyi bound is not affected by the presence of the magnetic impurity.

In the BPS limit, the energy density (43) can be rewritten in the form

$$\varepsilon_{bps} = \left(\sqrt{2U} \mp \frac{\Delta}{2}\right)^2 - \frac{\Delta^2}{4} + 2h\left(\frac{d\alpha}{dr}\right)^2, \tag{54}$$

where U stands for the BPS potential in Eq. (47).

The potential can also be written as a function of ϕ_3 and Δ,

$$U(\phi_3, \Delta) = \frac{g^2 h}{2}\left(\phi_3 \pm \frac{\Delta}{g\sqrt{h}}\right)^2, \tag{55}$$

which spontaneously breaks the $SU(3)$ symmetry inherent to the model (36), as expected. Also, the expression in Eq. (55) reveals that the presence of the magnetic impurity in the original Lagrangian density (36) requires an adjustment of the potential (in comparison to the model *without* the impurity) to support the existence of first-order configurations.

In the next section, we consider a localized magnetic impurity of the Gaussian type, from which we solve the BPS equations (51) and (52) numerically by means of a finite-difference scheme according to the boundary conditions (41) and (42).

A. Maxwell-$CP(2)$ vortex-like solitons: Numerical analysis

In order to continue, we need to choose an explicit expression for the localized magnetic impurity. For the sake of convenience, we prefer to work with a Gaussian profile centered at the origin, i.e.,

$$\Delta(r) = ce^{-dr^2}, \tag{56}$$

where both c and $d \in \mathbb{R}$, with $d > 0$. In this case, the parameters c and d control the height and width of the impurity, respectively.

Now, given the impurity (56), the first-order potential (47) can be written as

$$U = \frac{g^2 h^2}{2}\left(\cos\alpha \pm \frac{c}{gh}e^{-dr^2}\right)^2, \tag{57}$$

in which the upper (lower) sign holds for negative (positive) values of m (the winding number). In this manuscript, we consider the case with $d = 1$ and different values for c given that, as we explain later below, this case gives rise to interesting modifications of the profiles of the resulting first-order solutions.

In view of the potential (57), the first-order equations (51) and (52) take the form

$$\frac{1}{r}\frac{dA}{dr} = \mp g^2 h\left(\cos\alpha \pm \frac{c}{gh}e^{-dr^2}\right), \tag{58}$$

$$\frac{d\alpha}{dr} = \mp \frac{(2m - A)}{2r}\sin\alpha, \tag{59}$$

which must be solved according the boundary conditions (41) and (42). Here, we have also used Eq. (40) for the magnetic field.

In order to solve the above first-order equations numerically, we fix $g = h = 1$, for simplicity. Furthermore, we choose $m = 1$ (i.e., lower signs in the first-order expressions) and $d = 1$ (a fixed value for the width of the impurity). We then study the resulting first-order equations through a finite-difference algorithm for different values of c (the height of the impurity). Subsequently, we depict the numerical profiles for the profile functions $\alpha(r)$ and $A(r)$, the magnetic field $B(r)$ and the energy density $\varepsilon_{bps}(r)$.

Figure 1 shows the field profiles $\alpha(r)$ and $A(r)$ for $c = -5$ (dashed orange line), $c = -4$ (dashed red line), $c = -2$ (dashed blue line), $c = 0$ (usual solution, no impurity, solid black line), $c = +2$ (solid blue line), and $c = +4$ (solid red line). It is important to point out that the field profiles lose the original monotonicity (attained in the *absence* of impurity) as the value of $|c|$ increases. As a consequence, the profiles for α and A present a global maximum for $c = -4$ and $c = -5$, while A presents a global minimum for $c = 2$ and $c = 4$.

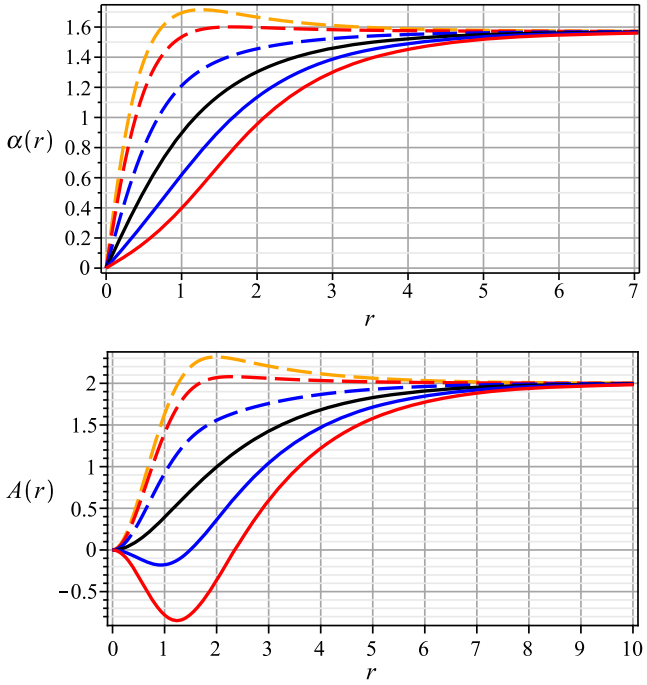

FIG. 1. Numerical solutions to $\alpha(r)$ (top) and $A(r)$ (bottom) coming from Eqs. (58) and (59) in the presence of Eqs. (41) and (42). Here, we have fixed $g = h = 1$, $m = 1$ (lower signs in the first-order expressions) and $d = 1$. This figure shows the profiles for $c = -5$ (dashed orange line), $c = -4$ (dashed red line), $c = -2$ (dashed blue line), $c = 0$ (usual solution, no impurity, solid black line), $c = +2$ (solid blue line), and $c = +4$ (solid red line).

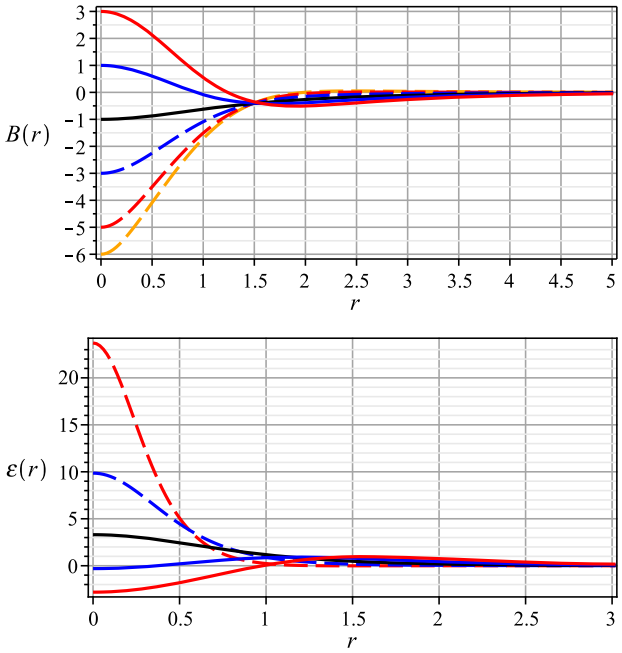

FIG. 2. Numerical solutions to the magnetic field $B(r)$ (top) and the energy density $\varepsilon(r)$ (bottom) of the first-order BPS Maxwell-$CP(2)$ configurations. Conventions as in the Fig. 1.

In Fig. 2, we depict the solutions for both the magnetic field $B(r)$ and the BPS energy density ε_{bps}. The profiles suggest that the parameter c (the height of the impurity) induces an inversion of the sign of both the magnetic field and the BPS energy density as these solutions approach the origin. In particular, for $c > 0$, the BPS energy density reaches negative values within a finite spatial region beginning at $r = 0$. The negative values arise due to the magnetic impurity which avoids to express the BPS energy density (43) as a sum of positive terms only; see Eq. (54).

1. Behavior of the solutions near the origin

To explain the sign inversion of the magnetic field and the BPS energy density near the origin, we first study the behavior of the profile functions $\alpha(r)$ and $A(r)$ themselves. In this sense, for $m > 0$, the field profiles when $r \to 0$ behave as (here, $C_0 > 0 \in \mathbb{R}$)

$$\alpha(r) \approx C_0 r^m, \tag{60}$$

$$A(r) \approx \frac{g^2 h}{2}\left(1 - \frac{c}{gh}\right) r^2, \tag{61}$$

which promptly recover the usual results for $c = 0$ (i.e., in the absence of the magnetic impurity).

We see that the impurity does not change the behavior of the scalar profile function $\alpha(r)$ near the origin. However, the impurity (via its height parameter c) changes the factor which multiplies the relevant term in the approximate solution for the gauge profile function $A(r)$.

In order to present the behavior of both the magnetic field and the BPS energy density near the origin, we consider $g = h = 1$, $m = 1$, and $d = 1$ (i.e., the values of the parameters used to obtain the numerical solutions). Then, we get the following behavior for the magnetic field:

$$B(r) \approx c - 1 + \frac{C_0^2 - 2c}{2} r^2. \tag{62}$$

For the BPS energy density, we obtain

$$\varepsilon_{bps}(r) \approx -c + 1 + 2C_0^2 + \frac{C_1}{6} r^2, \tag{63}$$

where $C_1 = 3c(3C_0^2 + 2) - 4C_0^2(C_0^2 + 3)$. We observe that both of these expressions reflect the behavior presented in Fig. 2, for $r \to 0$.

2. Behavior of the solutions in the asymptotic limit

We also present the behavior of the profile fields $\alpha(r)$ and $A(r)$ for large values of the radial coordinate. In the present case, for all values of c and d in Eq. (56), we find that the behaviors of the field profiles are

$$\alpha(r) \approx \frac{\pi}{2} - C_\infty \frac{\exp(-Mr)}{\sqrt{r}}, \tag{64}$$

$$A(r) \approx 2m - 2MC_\infty \sqrt{r}\exp(-Mr), \tag{65}$$

where C_∞ stands for a positive real constant and

$$M = g\sqrt{\frac{h}{2}}, \tag{66}$$

which is the mass of both the scalar and gauge bosons. We then conclude that the bosonic fields acquire the same mass in the self-dual limit, as in the Maxwell-Higgs model.

Therefore, the expressions (64) and (65) reveal that, in the presence of a localized magnetic impurity, the resulting first-order vortices mimic the standard asymptotic behavior, i.e., a localized impurity does not change the way the fields behave in the asymptotic region.

B. Topologically trivial solution: The $m = 0$ case

We now discuss the configuration characterized by a null topological charge in the presence of the same impurity already defined in Eq. (56). In the limit $d \to \infty$ and $c \to \infty$, with the ratio $c/d = \gamma > 0$ fixed (i.e., $c = \gamma d$), we get that

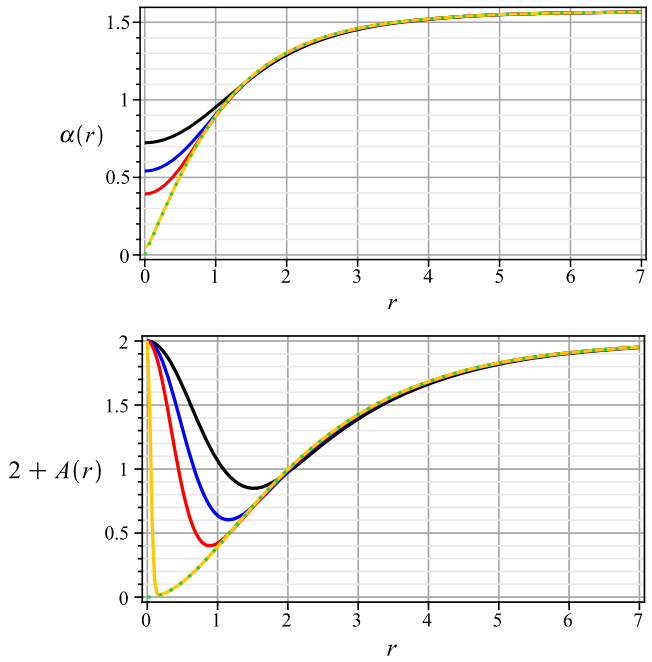

FIG. 3. Numerical solutions to $\alpha(r)$ (top) and $2 + A(r)$ (bottom) for $m = 0$ (i.e., the topologically trivial configuration). Here, we have depicted the solutions for $d = 1$ ($c = 4$, black line), $d = 2$ ($c = 8$, blue line), $d = 4$ ($c = 16$, red line), and $d = 256$ ($c = 1024$, orange line). The dotted green line represents the topological profile for $m = 1$ in the absence of the impurity.

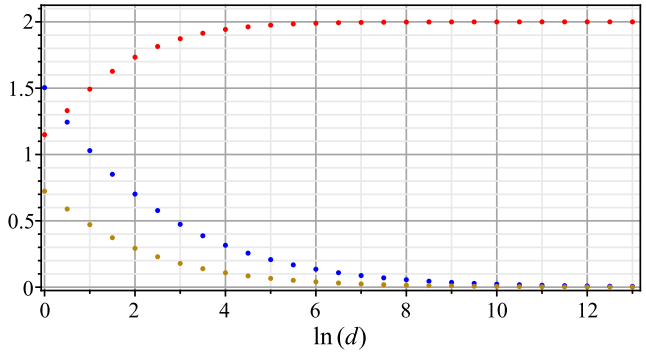

FIG. 4. The Maxwell-$CP(2)$ case with $m = 0$: this figure shows the behavior of $-A(r_{\min})$ (dotted red line), $r_{\min}$ (dotted blue line), and $\alpha(r = 0)$ (dotted golden line) *versus* $\ln(d)$. Here, $r_{\min}$ stands for the value of the radial coordinate for which the gauge profile function attains its minimum value, i.e., $A(r_{\min})$.

$$\lim_{d\to\infty} \gamma d \exp(-dr^2) = \gamma\pi\delta(r). \tag{67}$$

In the Ginzburg-Landau model, at critical coupling, with a δ-function impurity and $\gamma = 4$, the vortex with null topological charge behaves as a charge-1 vortex at critical coupling [28]. Surprisingly, this also remains true for axially symmetric configurations away from critical coupling [29].

Figure 3 shows the functions $\alpha(r)$ and $2 + A(r)$ for $c = 4d$ and $d = 1, 2, 4$, and 256. In general, as d increases, the shape of $\alpha(r)$ approaches that of a vortex with $m = 1$, while the minimum of the gauge field $A(r)$ tends to -2 and moves towards the origin (see Fig. 4). This can be compared to the gauge field of a vortex with $m = 1$ shifted by -2. Hence, we have showed numerically that the δ-function impurities also "behave" like vortices in this more sophisticated gauged-$CP(2)$ scenario. Moreover, while the profile function $\alpha(r)$ remains smooth, the gauge function $A(r)$ becomes singular in the limit $d \to \infty$ and develops a jump at the origin. We have also observed that, in general, when $c = 4md$, the limit $d \to \infty$ corresponds to a δ function of strength $4m\pi$ and the corresponding solution approaches a topological profile (in the lack of the impurity) with winding number m. Also in this case, the gauge profile function $A(r)$ maintains the jump at $r = 0$.

Figure 4 shows how the value of $\alpha(r = 0)$ (dotted golden line) goes to zero for large values of d, for $m = 0$ and $c = 4d$. The figure also shows how the value of $-A(r_{\min})$ approaches 2 whereas its localization $r_{\min}$ goes to zero (giving rise to the jump mentioned previously) for large values of d. This fact justifies the plot of $2 + A(r)$ in the bottom of Fig. 3.

IV. EFFECTIVE CHERN-SIMONS-$CP(2)$ MODEL

We now present the model which describes the interaction between the $CP(2)$ field and the Chern-Simons Abelian gauge one. The model is defined by the Lagrange density

$$\mathcal{L} = -\frac{\kappa}{4}\epsilon^{\alpha\mu\nu}A_\alpha F_{\mu\nu} + |\nabla_\mu\phi|^2 - V_0(\phi_3), \tag{68}$$

where the Chern-Simons term controls the gauge field's dynamics, while the parameter κ stands for the respective coupling constant. The basic definitions, conventions and correlated discussions introduced in Sec. II remain the same.

For the configuration (1), the effective model then reads

$$\mathcal{L} = -\frac{\kappa}{4}\epsilon^{\alpha\mu\nu}A_\alpha F_{\mu\nu} + |D_\mu\phi|^2 - V_0(\phi_3) - \lambda(h - \phi^\dagger\phi). \tag{69}$$

We are interested in the BPS structure that arises from the model above. In view of the Gauss law

$$\kappa B = -g^2 A_0|\psi|^2 = -\frac{1}{2}g^2 A_0(h - \phi_3^2), \tag{70}$$

the energy density takes the form

$$\varepsilon = \frac{\kappa^2 B^2}{g^2(h - \phi_3^2)} + (D_k\phi)^\dagger D_k\phi + V_0. \tag{71}$$

After some algebraic manipulations, the total energy of the effective system becomes

$$\begin{aligned}\mathcal{E} = \int d^2\mathbf{x}\Bigg\{&\frac{1}{2}|D_j\phi \pm i\epsilon_{jk}h^{-1/2}(\phi\times D_k\phi)^*|^2 \\ &+ \left(\frac{\kappa B}{g(h-\phi_3^2)^{1/2}} \mp \sqrt{V_0}\right)^2 \pm 2\pi h\bar{q}_0 \\ &\pm B\left(\frac{2\kappa\sqrt{V_0}}{g(h-\phi_3^2)^{1/2}} - h^{1/2}g\phi_3\right)\Bigg\},\end{aligned} \tag{72}$$

where $\bar{q}_0$ is the topological charge density defined in the previous Eq. (27). Again in this case, if we choose the factor which multiplies the magnetic field as zero, we determine the BPS potential of the model (69), i.e.,

$$V_0 = \frac{hg^2}{4\kappa^2}\phi_3^2(h - \phi_3^2), \tag{73}$$

via which we complete the implementation of the BPS formalism for the model (69) by writing the total energy as

$$\begin{aligned}\mathcal{E} = \mathcal{E}_{bps} &+ \int d^2\mathbf{x}\left(\frac{\kappa B}{g(h-\phi_3^2)^{1/2}} \mp \sqrt{V_0}\right)^2 \\ &+ \frac{1}{2}\int d^2\mathbf{x}|D_j\phi \pm ih^{-1/2}\epsilon_{jk}(\phi\times D_k\phi)^*|^2,\end{aligned} \tag{74}$$

where $\mathcal{E}_{bps}$ was defined in Eq. (28).

We see that total energy becomes equal to $\mathcal{E}_{bps}$ when the quadratic terms within the integrals are assumed to be zero, from which one gets the BPS or self-dual equations of the system, i.e.,

$$B = \pm\frac{h^{1/2}g^2}{2\kappa^2}\phi_3(h - \phi_3^2), \tag{75}$$

$$D_j\phi = \mp\, ih^{-1/2}\epsilon_{jk}(\phi\times D_k\phi)^*, \tag{76}$$

which mimic those inherent to the Chern-Simons-$O(3)$ sigma model. Furthermore, according to Refs. [36,37], the BPS system above is related to an extended supersymmetric version of the model (68).

In Ref. [10], the authors studied the rotationally symmetric solutions of the BPS system (75) and (76), for the case $\beta = \beta_1$. In the next section, we investigate the effects of a magnetic impurity on the BPS solitons supported by the model (69).

V. CHERN-SIMONS-$CP(2)$ VORTEX-LIKE SOLITONS IN THE PRESENCE OF A MAGNETIC IMPURITY

We now consider a second enlarged model which describes the interaction between the $CP(2)$-field and a Chern-Simons Abelian gauge one [i.e., a Chern-Simons-$CP(2)$ model]. The resulting model is defined by the Lagrange density

$$\mathcal{L} = -\frac{\kappa}{4}\epsilon^{\alpha\mu\nu}A_\alpha F_{\mu\nu} + |D_\mu\phi|^2 - V(\phi_3, \Delta) + \Delta B. \tag{77}$$

Also in this section, our study focuses on those time-independent configurations with radial symmetry. With such a purpose in mind, we again use the map defined by Eqs. (38) and (39) for the profile functions $\alpha(r)$ and $A(r)$ that still obey the boundary conditions (41) and (42). Besides, the scalar potential A_0 is also supposed to depend on the radial coordinate r only,

$$A_0 = A_0(r), \tag{78}$$

while the expressions for the magnetic and electric fields are

$$B(r) = -\frac{1}{gr}\frac{dA}{dr} \quad \text{and} \quad E(r) = -\frac{dA_0}{dr}, \tag{79}$$

respectively.

Here, as in the previous model, the term ΔB does not change the Gauss law (70) which comes from the Lagrange density (68) when considered in the absence of the impurity. So, one gets the Gauss law as

$$\kappa B = -\frac{g^2 h}{2}A^0\sin^2\alpha, \tag{80}$$

from which we get that the new model possesses configurations which carry both magnetic flux and electric charge

simultaneously, a well-known effect caused by the presence of the Chern-Simons term itself (see Ref. [10] and the discussion therein).

In what follows, we again focus our attention on those first-order solutions which minimize the total energy of the model. With such a purpose in mind, we implement the Bogomol'nyi prescription, the starting point being the radially symmetric expression for the energy density, which we write in a more convenient form as

$$\varepsilon = \frac{\kappa^2 B^2}{g^2 h \sin^2\alpha} + V(\alpha,\Delta) - \Delta B + h\left[\left(\frac{d\alpha}{dr}\right)^2 + \frac{(2m-A)^2}{4r^2}\sin^2\alpha\right], \tag{81}$$

where we have used the Gauss law (80) to express the scalar potential $A_0(r)$ as a function of the magnetic field $B(r)$.

Now, from Eq. (81), we initiate the implementation of the BPS technique providing, after some algebra, the following expression for the total energy:

$$\frac{\mathcal{E}}{2\pi} = \int_0^\infty \left[h\left(\frac{d\alpha}{dr} \pm \frac{(2m-A)}{2r}\sin\alpha\right)^2 + \left(\frac{\kappa B}{g\sqrt{h}\sin\alpha} \mp \sqrt{V}\right)^2 \pm 2\pi h \bar{q}_0 \pm B\left(\frac{2\kappa\sqrt{V}}{g h^{1/2}\sin\alpha} - hg\cos\alpha \mp \Delta\right)\right] r dr, \tag{82}$$

where the quantity $\bar{q}_0$ is the topological charge density of the model, being the same as that given in Eq. (46).

In order to complete the minimization of the total energy according to the Bogomol'nyi prescription, we set to zero the expression that multiplies the magnetic field in the third row of Eq. (82) it allow us to determine the BPS potential $V(\alpha,\Delta)$ as

$$V(\alpha,\Delta) = \frac{g^4 h^3}{4\kappa^2}\left(\cos\alpha \pm \frac{\Delta}{gh}\right)^2 \sin^2\alpha, \tag{83}$$

where both the potential and the function Δ go to zero when $r \to \infty$.

This way, the total energy becomes

$$\frac{\mathcal{E}}{2\pi} = \frac{\mathcal{E}_{bps}}{2\pi} + \int_0^\infty \left[\left(\frac{\kappa B}{g\sqrt{h}\sin\alpha} \mp \sqrt{V}\right)^2\right] r dr + h\int_0^\infty \left[\frac{d\alpha}{dr} \pm \frac{(2m-A)}{2r}\sin\alpha\right]^2 r dr, \tag{84}$$

where we have introduced the energy $\mathcal{E}_{bps}$ defined in Eq. (28) and whose value is the same one which appears in Eq. (49). Furthermore, from Eq. (84), we write the inequality

$$\mathcal{E} \geq \mathcal{E}_{bps}, \tag{85}$$

from which we clearly see that $\mathcal{E}_{bps}$ stands for the Bogomol'nyi bound which can be calculated in the very same way as before [i.e., via the use of the boundary conditions (41) and (42)]. The inequality (85) reveals that the Bogomol'nyi bound is saturated when the fields which appear in Eq. (84) satisfy the BPS equations:

$$B = \pm\frac{g^3 h^2}{2\kappa^2}\left(\cos\alpha \pm \frac{\Delta}{gh}\right)\sin^2\alpha, \tag{86}$$

$$\frac{d\alpha}{dr} = \mp\frac{(2m-A)}{2r}\sin\alpha, \tag{87}$$

whose solutions describe time-independent configurations with total energy given by $\mathcal{E} = \mathcal{E}_{bps} = 4\pi h|m|$, which is equal to the energy inherent to the BPS structures obtained in the previous Maxwell-$CP(2)$ case (see Sec. III and the discussion therein).

Furthermore, the BPS energy density obtained from Eq. (81) is

$$\varepsilon_{bps} = \left(\sqrt{2V} \mp \frac{\Delta}{2}\right)^2 - \frac{\Delta^2}{4} + 2h\left(\frac{d\alpha}{dr}\right)^2, \tag{88}$$

with the BPS potential V given by Eq. (83). The latter can be rewritten in terms of ϕ_3 as

$$V(\phi_3,\Delta) = \frac{g^4 h}{4\kappa^2}\left(\phi_3 \pm \frac{\Delta}{g\sqrt{h}}\right)^2 (h - \phi_3^2), \tag{89}$$

which allows the spontaneous breaking of the $SU(3)$ symmetry inherent to the original Chern-Simons-$CP(2)$ model, as expected.

Below, we investigate the first-order equations (86) and (87) numerically. In the sequence, we plot the resulting BPS profiles and comment on their main properties engendered by the presence of a localized impurity.

A. Chern-Simons-$CP(2)$ vortex-like solitons: Numerical results

In the sequence, we choose the localized magnetic impurity as in Eq. (56), i.e.,

$$\Delta(r) = ce^{-dr^2}, \tag{90}$$

via which we rewrite the potential (83) in the form

$$V(\alpha,\Delta) = \frac{g^4 h^3}{4\kappa^2}\left(\cos\alpha \pm \frac{c}{gh}e^{-dr^2}\right)^2 \sin^2\alpha. \tag{91}$$

In this sense, the BPS equations (86) and (87) become

$$\frac{1}{r}\frac{dA}{dr} = \mp\frac{g^4 h^2}{2\kappa^2}\left(\cos\alpha \pm \frac{c}{hg}e^{-dr^2}\right)\sin^2\alpha, \tag{92}$$

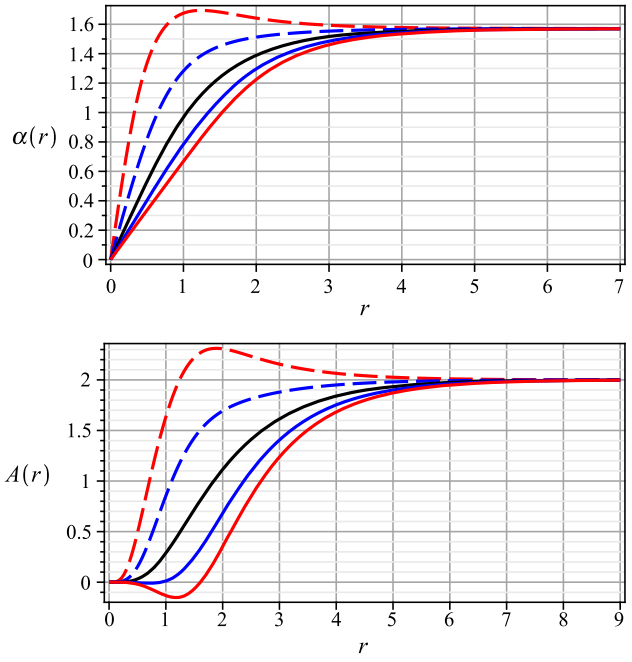

FIG. 5. Numerical solutions to $\alpha(r)$ (top) and $A(r)$ (bottom) coming from Eqs. (92) and (93) in the presence of Eqs. (41) and (42). The results hold for $\kappa = h = m = 1$, $g = \sqrt{2}$, $d = 1$, and $c = -4$ (dashed red line), $c = -2$ (dashed blue line), $c = 0$ (solution without magnetic impurity, solid black line), $c = +2$ (solid blue line), and $c = +4$ (solid red line).

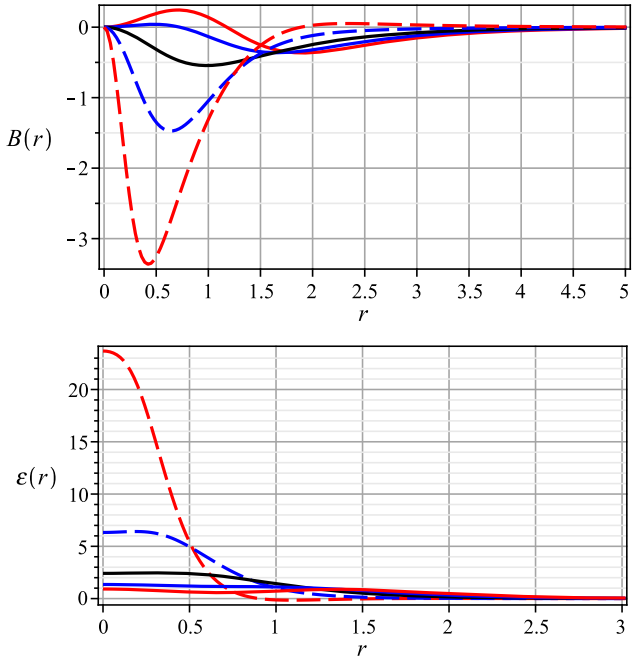

FIG. 6. Numerical solutions to the magnetic field $B(r)$ (top) and the energy density $\varepsilon_{bps}(r)$ (bottom) of the first-order Chern-Simons-$CP(2)$ configurations. Conventions are as in Fig. 5.

$$\frac{d\alpha}{dr} = \mp \frac{(2m - A)}{2r} \sin\alpha, \tag{93}$$

whose solutions must satisfy the boundary conditions (41) and (42). As in Sec. II, we only consider the lower signs in the BPS equations in order to describe the first-order solutions for $m > 0$.

We again implement a finite-difference algorithm in order to solve the first-order equations (92) and (93) numerically. In this sense, we choose $\kappa = h = 1$, $g = \sqrt{2}$, $m = 1$, $d = 1$ (the impurity's "width"), from which we study the BPS configurations for the same values of c (the impurity's "height") already considered in Sec. III, i.e., $c = -4$ (dashed red line), $c = -2$ (dashed blue line), $c = 0$ (usual solution, no impurities, solid black line), $c = +2$ (solid blue line), and $c = +4$ (solid red line). We depict the numerical solutions for the relevant fields in Figs. 5–7. Here, it is important to say that the solution for $c = -5$ is not shown because the effects caused by the impurity can be seen clearly in the profile for $c = -4$.

Figure 5 shows the solutions to the profile functions $\alpha(r)$ and $A(r)$, from which one notes that the same effects are again present when the values of $|c|$ increase, i.e., the profiles lose their monotonicity because of the presence of the magnetic impurity. In particular, due to the loss of monotonicity, the $\alpha(r)$ profiles can assume values that are eventually bigger than $\pi/2$.

Figure 6 depicts the magnetic field $B(r)$ and the energy density ε_{bps}. For increasing values of $|c|$, we again identify an inversion on the sign (i.e., a flip) of the magnetic field as already observed in the previous model, such an effect is

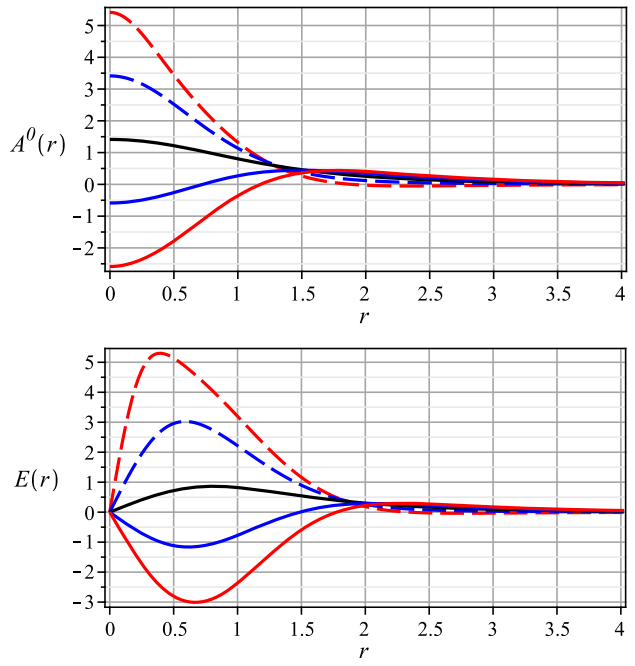

FIG. 7. Numerical solutions to the scalar potential $A^0(r)$ (top) and the electric field $E(r)$ (bottom) of the first-order Chern-Simons-$CP(2)$ configurations. Conventions are as in Fig. 5.

caused by the magnetic impurity which gives rise to a gauge field with a nonmonotonic shape. Moreover, despite the effects caused by the impurity, the energy density remains localized and well behaved along the radial coordinate, as expected.

Finally, we plot the profiles for the scalar potential $A^0(r)$ and the electric field $E(r) = -dA_0/dr$ in Fig. 7. The Gauss law (80) defines a linear dependence between the scalar potential and the magnetic field, which means that the flipping of B (see Fig. 5) leads to an inversion of the sign of A^0, and vice versa. Hence, the scalar potential's nonmonotonic behavior also produces the sign inversion of the electric field itself.

1. Behavior of the solutions near the origin

We now investigate the way that the profile fields $\alpha(r)$ and $A(r)$ approach the values (41) and (42). Without loss of generality, we consider only those configurations with positive values of the winding number m. Thus, the behaviors of the profile functions near the origin are

$$\alpha(r) \approx \mathcal{C}_0 r^m, \tag{94}$$

$$A(r) \approx \frac{\mathcal{C}_0^2 g^3 h(hg-c)}{4\kappa^2(m+1)} r^{2(m+1)}, \tag{95}$$

where $\mathcal{C}_0$ stands for a positive real constant.

We write below the behaviors near the origin for the magnetic field, the BPS energy density, the scalar potential, and the electric field. For such a purpose, we consider $\kappa = h = 1$, $g = \sqrt{2}$, $m = 1$, and $d = 1$, i.e., the same values used to obtain the previous numerical solutions. Then, we get the following behavior for the magnetic sector:

$$B(r) \approx \mathcal{C}_0^2(c-\sqrt{2})r^2. \tag{96}$$

For the BPS energy density, we obtain

$$\varepsilon_{bps}(r) \approx 2\mathcal{C}_0^2 - \frac{\mathcal{C}_1}{3} r^2, \tag{97}$$

where $\mathcal{C}_1 = \mathcal{C}_0^2(3\sqrt{2}c + 2\mathcal{C}_0^2 - 6)$.

As a result, the expressions above offer an explanation in terms of the values of c about the behavior of the corresponding sectors near the origin which appear in Fig. 6.

Further, the behaviors of the scalar potential and electric field become

$$A_0(r) \approx \sqrt{2} - c + \left(c - \frac{\sqrt{2}}{2}\mathcal{C}_0^2\right) r^2, \tag{98}$$

$$E(r) \approx (\sqrt{2}\mathcal{C}_0^2 - 2c)r - \frac{\sqrt{2}\mathcal{C}_0^4 - 6c}{3} r^3, \tag{99}$$

respectively. These approximate solutions also explain the behaviors near $r = 0$ depicted in Fig. 7.

2. Behavior of the solutions in the asymptotic limit

On the other hand, in the asymptotic limit $r \to \infty$, the fields behave as

$$\alpha(r) \approx \frac{\pi}{2} - \mathcal{C}_\infty \frac{\exp(-\mathcal{M}r)}{\sqrt{r}}, \tag{100}$$

$$A(r) \approx 2m - 2\mathcal{M}\mathcal{C}_\infty \sqrt{r}\exp(-\mathcal{M}r), \tag{101}$$

for all of the values of c and d in Eq. (90), where C_∞ stands for a positive real constant and

$$\mathcal{M} = \frac{g^2 h}{2\kappa} \tag{102}$$

represents the mass of both of the bosons in the Bogomol'nyi limit. As in the Maxwell-$CP(2)$ case, it is also possible to conclude in the present Chern-Simons scenario that a localized impurity does not change the way that the profile functions approach their asymptotic values.

B. Topologically trivial solution: $m = 0$ case

We finally end this section by considering the nontopological ($m = 0$) configuration engendered by the δ-function impurity given in Eq. (67); see Sec. III B and the discussion therein.

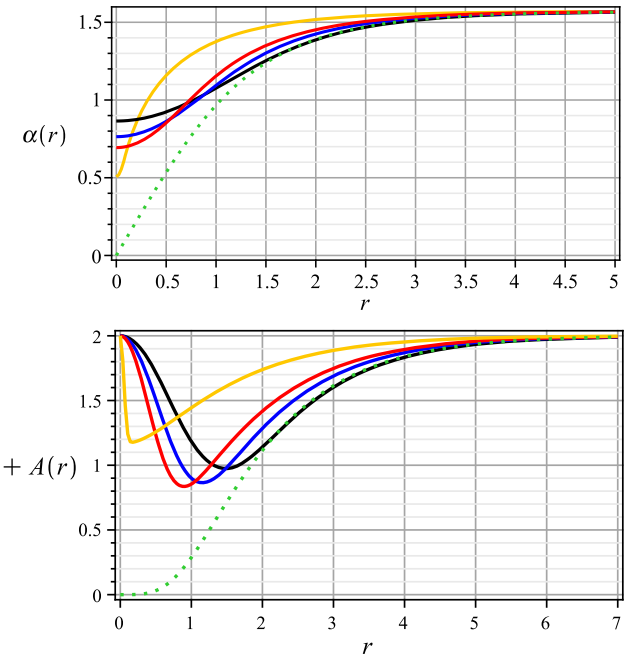

FIG. 8. Numerical solutions to $\alpha(r)$ (top) and $2 + A(r)$ (bottom) for $m = 0$ (i.e., the vacuum configuration). The impurity is still given by Eq. (90). Here, we depict the solutions for $d = 1$ ($c = 4$, black line), $d = 2$ ($c = 8$, blue line), $d = 4$ ($c = 16$, red line), and $d = 256$ ($c = 1024$, orange line). Again, the dotted green line stands for the topological profile with $m = 1$ in the absence of impurities.

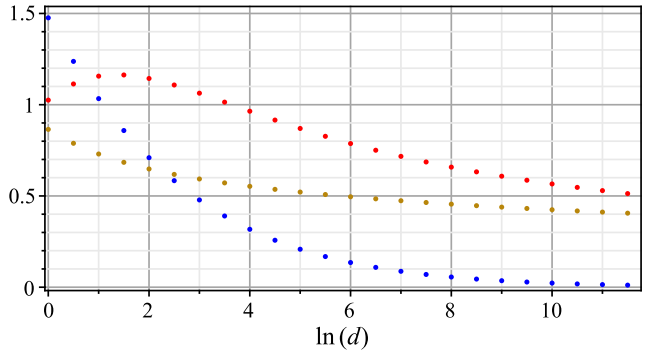

FIG. 9. The Chern-Simons-$CP(2)$ case: this figure shows the behavior of $-A(r_{\min})$ (dotted red line), $r_{\min}$ (dotted blue line), and $\alpha(r=0)$ (dotted golden line) *versus* $\ln(d)$. As in the previous case, $r_{\min}$ is the value of r for which the gauge profile function attains its minimum value.

The numerical results for the profile functions $\alpha(r)$ and $2+A(r)$ are shown in Fig. 8, again for $\gamma=4$ and $d=1,2,4$, and 256. We observe that in the present case the $m=0$ solution does not mimic the behavior previously found in the Maxwell-$CP(2)$ scenario, i.e., the profile for $\alpha(r)$ does not approach that of a $m=1$ topological vortex as d increases. At the same time, the minimum of $A(r)$ does not saturate to the value -2, but rather moves towards the origin; see Fig. 9. As a consequence, in the present Chern-Simon-$CP(2)$ case, the topologically trivial configuration does not behave as a $m=1$ vortex, which arises in the absence of the impurity.

VI. FINAL COMMENTS AND PERSPECTIVES

We have performed the construction of BPS vortices in the context of two different gauged-$CP(2)$ scenarios that were enlarged via an additional term which represents a magnetic impurity. With such an aim in mind, we chose a specific $CP(2)$ configuration [Eq. (1)] as being coupled to both the Maxwell and Chern-Simons fields, separately. Here, it is worth noting that such a configuration presents a $CP(2)$ topological charge which equals zero not only in the simplest (free) scenario, but also when the $CP(2)$ field is coupled to an Abelian gauge one. However, the BPS formalism shows that the effective models for Eq. (1) possess a self-dual structure which looks like that of the gauged sigma models. Moreover, the full implementation of the BPS technique allows us to fix the self-dual potentials in both the Maxwell and Chern-Simons cases; see Eqs. (47) and (83), respectively. In this sense, we have verified that the magnetic impurity contributes explicitly to the self-dual potentials and appears in both models' BPS equations. The interesting point is that the impurity does not change the Bogomol'nyi bounds saturated by the BPS configurations, i.e., the corresponding self-dual energies remain quantized according to the winding number m, as expected for topological structures.

In order to study the effects caused by the magnetic impurity on the solutions of the BPS systems, we have particularized our analysis by choosing a Gaussian (localized) impurity controlled by two real parameters, c and d (which control the "height" and the "width" of the impurity, respectively). For a fixed value of d and different values of c, the numerical analysis demonstrated how the parameter c induces not only the loss of monotonicity of the profile functions $\alpha(r)$ and $A(r)$, but also the flipping of both the magnetic and electric fields. The analysis of the behavior near the origin explained both peculiarities. In addition, we verified that the impurity does not change the manner in which these fields behave in the asymptotic region (i.e., $r\to\infty$).

Based on the results that we have introduced in this work, an interesting issue to be studied in the future is the effect eventually caused by a localized impurity on the shape of nontopological BPS Chern-Simons-$CP(2)$ vortices. Another point which claims for a future analysis includes the study of the interaction between a moving gauged-$CP(2)$ vortex and a static magnetic impurity. The results of these topics, currently under investigation, will be reported elsewhere.

ACKNOWLEDGMENTS

This work was financed in part by the Coordenação de Aperfeiçoamento de Pessoal de Nível Superior—Brasil (CAPES)—Finance Code 001, the Conselho Nacional de Pesquisa e Desenvolvimento Científico e Tecnológico—CNPq and the Fundação de Amparo à Pesquisa e ao Desenvolvimento Científico e Tecnológico do Maranhão—FAPEMA (Brazilian agencies). In particular, V. A. thanks the full support from CAPES (via a Ph.D. scholarship). R. C. acknowledges the support from the Grants No. CNPq/306724/2019-7, No. CNPq/423862/2018-9, No. FAPEMA/Universal-01131/17, and No. FAPEMA/Universal-00812/19. E. H. thanks the support from the grants No. CNPq/307545/2016-4, No. CNPq/309604/2020-6 and No. FAPEMA/COOPI/07838/17. S. K. would like to thank Jack McKenna and Abera Muhamed for interesting discussions. E. H. also acknowledges the School of Mathematics, Statistics and Actuarial Science of the University of Kent (Canterbury, United Kingdom) for the kind hospitality during the realization of part of this work.

[1] N. Manton and P. Sutcliffe, *Topological Solitons* (Cambridge University Press, Cambridge, England, 2004).
[2] E. Bogomol'nyi, Sov. J. Nucl. Phys. **24**, 449 (1976); M. Prasad and C. Sommerfield, Phys. Rev. Lett. **35**, 760 (1975).
[3] H. J. de Vega and F. A. Schaposnik, Phys. Rev. D **14**, 1100 (1976).
[4] A. N. Atmaja, H. S. Ramadhan, and E. da Hora, J. High Energy Phys. 02 (2016) 117.
[5] H. B. Nielsen and P. Olesen, Nucl. Phys. **B61**, 45 (1973).
[6] R. Jackiw and E. J. Weinberg, Phys. Rev. Lett. **64**, 2234 (1990); R. Jackiw, K. Lee, and E. J. Weinberg, Phys. Rev. D **42**, 3488 (1990).
[7] C. Lee, K. Lee, and H. Min, Phys. Lett. B **252**, 79 (1990).
[8] A. Yu. Loginov, Phys. Rev. D **93**, 065009 (2016).
[9] R. Casana, M. L. Dias, and E. da Hora, Phys. Lett. B **768**, 254 (2017).
[10] V. Almeida, R. Casana, and E. da Hora, Phys. Rev. D **97**, 016013 (2018); R. Casana, M. L. Dias, and E. da Hora, Phys. Rev. D **98**, 056011 (2018).
[11] R. Casana, N. H. Gonzalez-Gutierrez, and E. da Hora, Europhys. Lett. **127**, 61001 (2019).
[12] R. Casana, M. L. Dias, and E. da Hora, Phys. Rev. D **96**, 076013 (2017).
[13] J. Andrade, R. Casana, E. da Hora, and C. dos Santos, Phys. Rev. D **99**, 056014 (2019).
[14] T. Shapoval, V. Metlushko, M. Wolf, B. Holzapfel, V. Neu, and L. Schultz, Phys. Rev. B **81**, 092505 (2010).
[15] S. Tung, V. Schweikhard, and E. A. Cornell, Phys. Rev. Lett. **97**, 240402 (2006).
[16] P. W. Anderson and N. Itoh, Nature (London) **256**, 25 (1975).
[17] A. Bulgac, M. M. Forbes, and R. Sharma, Phys. Rev. Lett. **110**, 241102 (2013).
[18] G. Wlazłowski, K. Sekizawa, P. Magierski, A. Bulgac, and M. M. Forbes, Phys. Rev. Lett. **117**, 232701 (2016).
[19] C. Adam and A. Wereszczynski, Phys. Rev. D **98**, 116001 (2018).
[20] C. Adam, J. M. Queiruga, and A. Wereszczynski, J. High Energy Phys. 07 (2019) 164.
[21] S. W. Goatham, L. E. Mannering, R. Hann, and S. Krusch, Acta Phys. Pol. B **42**, 2087 (2011).
[22] N. S. Manton, Ann. Phys. (N.Y.) **256**, 114 (1997).
[23] N. M. Romao and J. M. Speight, Nonlinearity **17**, 1337 (2004).
[24] S. Krusch and P. Sutcliffe, Nonlinearity **19**, 1515 (2006).
[25] D. Tong and K. Wong, J. High Energy Phys. 01 (2014) 090.
[26] X. Han and Y. Yang, Nucl. Phys. **B898**, 605 (2015); R. Zhang and H. Li, Nonlinear Anal. **115**, 117 (2015).
[27] X. Han and Y. Yang, J. High Energy Phys. 02 (2016) 046.
[28] A. Cockburn, S. Krusch, and A. A. Muhamed, J. Math. Phys. (N.Y.) **58**, 063509 (2017).
[29] J. E. Ashcroft and S. Krusch, Phys. Rev. D **101**, 025004 (2020).
[30] K. Aoki, K. Sakakibara, I. Ichinose, and T. Matsui, Phys. Rev. B **80**, 144510 (2009).
[31] C. Wu, J. Hu, and S. Zhang, Phys. Rev. Lett. **91**, 186402 (2003).
[32] H. T. C. Stoof, E. Vliegen, and U. Al Khawaja, Phys. Rev. Lett. **87**, 120407 (2001).
[33] D. E. Chang, Phys. Rev. A **66**, 025601 (2002).
[34] K. Kasamatsu, M. Tsubota, and M. Ueda, Int. J. Mod. Phys. B **19**, 1835 (2005).
[35] Along the present manuscript, the metric signature is considered as $\eta_{\mu\nu} = (+--)$. Moreover, Greek indices represent space-time coordinates, while the Latin ones label spatial coordinates only. Here, we also use the Natural Units System.
[36] E. Witten and D. Olive, Phys. Lett. **78B**, 97 (1978).
[37] Z. Hlousek and D. Spector, Nucl. Phys. **B370**, 143 (1992).